

Multifunctional Antireflection Coatings Based on Novel Hollow Silica–Silica Nanocomposites

Xianpeng Zhang,[†] Pinjun Lan,[†] Yuehui Lu,^{†,*} Jia Li,[†] Hua Xu,[‡] Jing Zhang,[†] YoungPak Lee,[§] Joo Yull Rhee,[†] Kwang-Leong Choy,[#] and Weijie Song^{*,†}

[†]Ningbo Institute of Material Technology and Engineering, Chinese Academy of Sciences, Ningbo 315201, China

[‡]Department of Physics, Faculty of Science, Ningbo University, Ningbo 315211, China

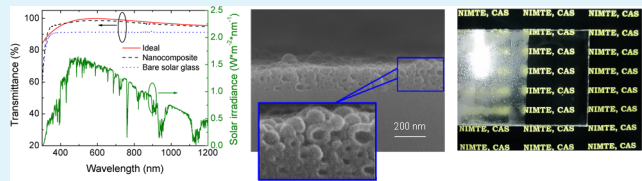
[§]Quantum Photonic Science Research Center and Department of Physics, Hanyang University, Seoul 133-791, South Korea

[#]Department of Physics, Sungkyunkwan University, Suwon 440-746, South Korea

^{*}Faculty of Engineering, The University of Nottingham, University Park, Nottingham NG7 2RD, United Kingdom

Supporting Information

ABSTRACT: Antireflection (AR) coatings that exhibit multifunctional characteristics, including high transparency, robust resistance to moisture, high hardness, and antifogging properties, were developed based on hollow silica–silica nanocomposites. These novel nanocomposite coatings with a closed-pore structure, consisting of hollow silica nanospheres (HSNs) infiltrated with an acid-catalyzed silica sol (ACSS), were fabricated using a low-cost sol–gel dip-coating method. The refractive index of the nanocomposite coatings was tailored by controlling the amount of ACSS infiltrated into the HSNs during synthesis. Photovoltaic transmittance (T_{PV}) values of 96.86–97.34% were obtained over a broad range of wavelengths, from 300 to 1200 nm; these values were close to the theoretical limit for a lossy single-layered AR coating (97.72%). The nanocomposite coatings displayed a stable T_{PV} , with degradation values of less than 4% and 0.1% after highly accelerated temperature and humidity stress tests, and abrasion tests, respectively. In addition, the nanocomposite coatings had a hardness of approximately 1.6 GPa, while the porous silica coatings with an open-pore structure showed more severe degradation and had a lower hardness. The void fraction and surface roughness of the nanocomposite coatings could be controlled, which gave rise to near-superhydrophilic and antifogging characteristics. The promising results obtained in this study suggest that the nanocomposite coatings have the potential to be of benefit for the design, fabrication, and development of multifunctional AR coatings with both omnidirectional broadband transmission and long-term durability that are required for demanding outdoor applications in energy harvesting and optical instrumentation in extreme climates or humid conditions.



KEYWORDS: *multifunctional, antireflection coatings, hollow silica, nanocomposites, durability, antifogging*

INTRODUCTION

Various coatings on glass have been developed in order to achieve a variety of functional characteristics, including antireflective,^{1,2}抗scratches, antifogging, and self-cleaning properties. For example, Chiang et al. reported that the use of zeolite coatings can provide the antireflective and抗scratches characteristics.³ Laroche et al. developed a polymer-based antifogging coating that was covalently grafted onto glass surfaces using a multistep process.⁴ Yang et al. reported the use of nanopatterning to create self-cleaning and antireflective surfaces on glass.⁵

Conventional dense single-layered antireflection (SLAR) coatings are able to suppress Fresnel reflection arising from the different refractive indices of air and glass,¹ thus improving the conversion efficiency of photovoltaic (PV) modules.^{6,7} However, such dense coatings with a quarter-wave optical thickness can only eliminate partial reflection at a specific wavelength. Hence, various multilayered,^{8–10} gradient refractive-index,^{11–13} and nanopatterned^{14,15} antireflection (AR)

coatings have been developed to extend and optimize the low-reflectance regime. In an alternative approach, porous SLAR coatings with a refractive index even lower than the lowest possible refractive index for dense AR coatings (i.e., $n_{\text{MgF}_2} \approx 1.38$) are widely used in industry for the encapsulated solar glass in photovoltaic (PV) modules.^{16,17} Such porous SLAR coatings exhibit high transmittance over a broad range of wavelengths, and they can be manufactured on large-area glass substrates at low cost.^{18–21}

However, the solar glass used in PV modules often encounters moisture, rain, and high temperatures (typically, constant temperatures of between 21 and 53 °C, and maximum temperatures of 75 and 96 °C for rack-mounted and roof-mounted modules, respectively) during operation, which can

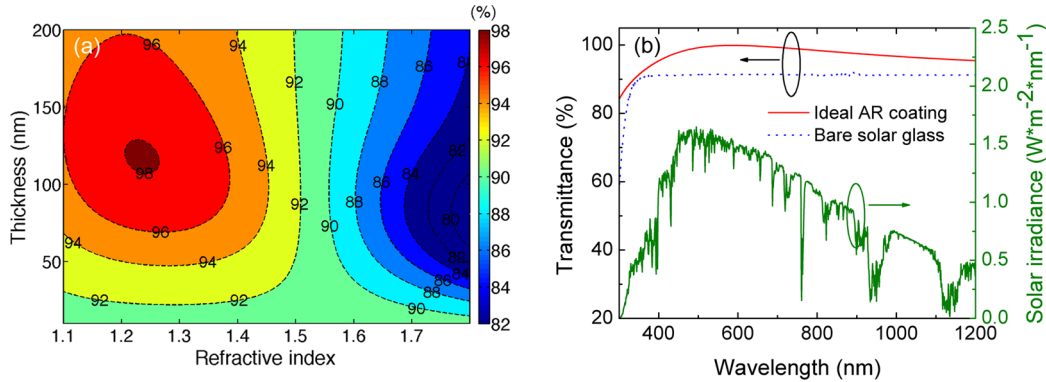


Figure 1. (a) Contour plot of the PV transmittance, T_{PV} , as a function of the thickness and refractive index of the SLAR coating. (b) Calculated transmittance spectra of an ideal lossless SLAR coating (with a thickness of 118 nm and a refractive index of 1.23) and a bare solar glass, overlaid with the solar spectral irradiance at AM1.5.

lead to the irreversible corrosion of the glass and the degradation of the transmission; these detrimental processes arise from ion exchange and/or network dissolution.^{22,23} AR coatings on solar glass must therefore be able to resist external weathering and protect the solar glass, as well as suppress reflection over a broad range of wavelengths,^{3,24–27} because of the nature of the solar irradiance spectrum. Unfortunately, the porous surface of AR coatings is prone to adsorb contaminants, giving rise to the variations in the refractive index and degradation of the transmission, as well as poor mechanical reliability in the porous films, which are the major bottlenecks preventing the practical use of AR-coated solar glass in PV modules.^{4,15,28,29} A certain porosity (~50%) must be preserved in AR coatings, because it is responsible for the broadband antireflection originating from the low refractive index of ~1.22. However, the high porosity of these AR coatings would bring about the poor durability. These conflicting requirements mean that the practical design and fabrication of AR coatings remains highly challenging. Boilot et al.¹⁹ suggested that a possible solution could be to transform the open pores into closed pores with a diameter of 30–100 nm, thus avoiding the adsorption of moisture and capillary condensation. Fortunately, there have been the studies to synthesize hollow nanoparticles,^{30–33} which could be good candidate building blocks for SLAR coatings. Rubner et al.³⁴ demonstrated that AR coatings made from hollow silica nanospheres (HSNs) with closed-pores using a sacrificial template method unambiguously decreased the reflection over the wavelength range from the near-ultraviolet to the visible. He et al.³⁵ fabricated hollow mesoporous silica nanospheres (i.e., with open and closed pores) using LbL dip-coating, and these materials produced a significant reduction in the reflection from the visible to the near-infrared regions. However, to date, it has proven difficult to control the desired refractive index precisely using the sacrificial template approach.

Moreover, the optical function and the specified wettability are confined to a simple pairwise integration of two distinct fields.³⁶ For example, Jiang et al. demonstrated that the templated silicon and glass subwavelength pillar arrays could be conferred with antireflective and superhydrophobic characteristics by functionalizing them with fluorosilane via a silane coupling reaction.³⁷ If a multifunctional single-layered coating system could be developed to provide coatings with the desired functional characteristics (i.e., a combination of antireflective,抗scratches, antifogging, damp-proof, and self-cleaning properties), it would simplify the processing and reduce the cost of

coated glass. Such coated glass would be highly desirable for practical engineering applications such as energy harvesting, and for use in optical instrumentation in extreme climates or humid conditions. Although some effort has been dedicated to the realization of multifunctional coatings,^{38,39} such studies are very limited at present.

To avoid the complexity of sacrificial template removal during the synthesis of HSNs and achieve high transmission (over the range of $\lambda = 300$ –1200 nm) with superior durability and inherent wettability, we developed a facile strategy to prepare novel silica–silica nanocomposite SLAR coatings on solar glass using a sol–gel dip-coating method. These new composite materials, consisting of HSNs synthesized using a poly(acrylic acid) (PAA) template and an acid-catalyzed silica sol (ACSS) infiltrated into the HSNs, which acted as a binder and a regulator of the refractive index, provided more degrees of freedom for the control of the optical and surface wetting properties. By varying the amount of ACSS, the refractive index was tuned to an optimum value that was found from PV-transmittance oriented numerical calculations, which allowed a significant improvement in the antireflection properties of the silica–silica nanocomposite SLAR coatings to be achieved. The durability of the coatings was studied using a highly accelerated temperature and humidity stress test (HAST) and a nano-indenter measurement. The surface wettability was investigated using a time-dependent water contact angle (WCA) measurement, and the antifogging characteristics of the coatings were also demonstrated.

THEORETICAL DESIGN

The PV transmittance, T_{PV} , was introduced to evaluate the transmittance of solar irradiance; T_{PV} is a weighted average transmittance, and can be defined as follows^{40,41}

$$T_{PV} = \frac{\sum_{\lambda_{\min}}^{\lambda_{\max}} T(\lambda) S_{\lambda} \Delta \lambda}{\sum_{\lambda_{\min}}^{\lambda_{\max}} S_{\lambda} \Delta \lambda} \quad (1)$$

where λ_{\min} , λ_{\max} , $T(\lambda)$, $S(\lambda)$, and $\Delta \lambda$ are the shortest wavelength, the longest wavelength, the wavelength-dependent transmittance, the solar irradiance intensity, and the wavelength increment, respectively. Similarly, the PV reflectance, R_{PV} , could be calculated by replacing $T(\lambda)$ in eq 1 with $R(\lambda)$.

By varying the thickness and the refractive index of the SLAR coatings from 10 to 200 nm and 1.1 to 1.8, respectively, excluding the dispersion and absorption for simplicity, high T_{PV}

Table 1. Calculated and Measured T_{PV} and R_{PV} ; Improvements in T_{PV} and R_{PV} Relative to the Values for the Bare Solar Glass (which are shown in parentheses)

case	calcd T_{PV} (%)	measured T_{PV} (%)	calcd R_{PV} (%)	measured R_{PV} (%)
solar glass	91.50	91.21	8.28	8.56
ideal ^a	98.09 (6.59)		0.55 (7.73)	
ideal with loss ^b	97.72 (6.22)		0.55 (7.73)	
$T = 450^{\circ}\text{C}$	97.50 (6.00)	97.28 (6.07)	0.61 (7.67)	2.27 (6.29)

^aIt corresponds to the maximum T_{PV} in Figure 1a, where the refractive index is 1.23 and the thickness is 118 nm. ^bThe parameters (i.e., refractive index and thickness) are the same as the ideal case except that the extinction coefficient is assumed to be that of nanocomposite SLAR coatings.

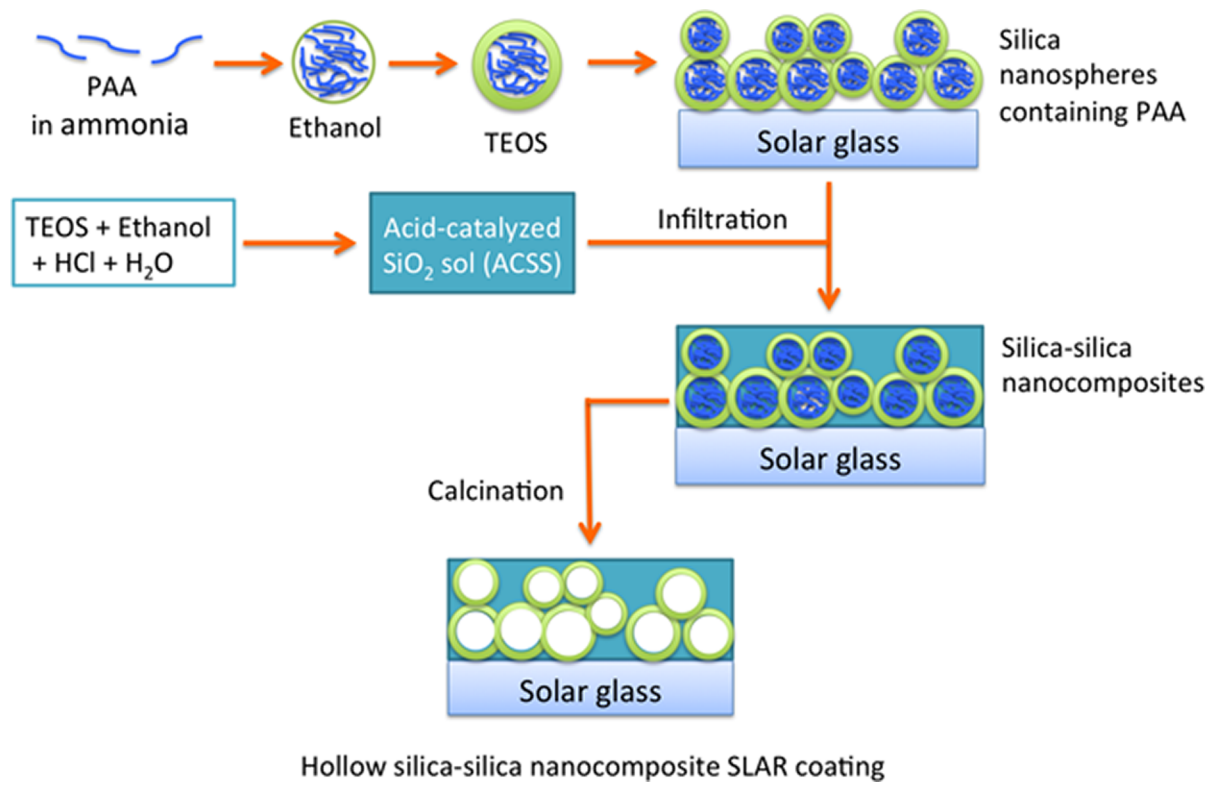


Figure 2. Schematic illustration of the preparation of the SLAR coatings, made from HSNs infiltrated by ACSS.

values of approximately 98% could be achieved, if the thickness was in the range of 108–123 nm and the refractive index was in the range of 1.21–1.26, as shown in Figure 1a. An ideal SLAR coating with the highest T_{PV} of 98.09% should have a thickness of 118 nm and a refractive index of 1.23. The transmittance spectrum of the ideal SLAR coating is shown in Figure 1b, overlaid with the solar spectral irradiance at AM1.5. The transmittance of the ideal SLAR coating was much higher than that of the bare solar glass, over the whole wavelength range. This was especially clear in the wavelength range of 400–700 nm; in this wavelength range T_{PV} showed an increase of 6.59% compared with the bare solar glass ($T_{PV} = 91.50\%$), as summarized in Table 1. This was because most solar irradiance is distributed in this wavelength region. Therefore, SLAR coatings with a thickness and a refractive index in the range of 108–123 nm and 1.21–1.26, respectively, could be beneficial for light harvesting in PV modules.

MATERIALS AND METHODS

To realize SLAR coatings with the previously described desirable properties, we implemented a facile, chemical solution-based, soft-template route to synthesize silica nanospheres containing the PAA template via a modified Stöber method.³⁵ ACSS was then infiltrated

into the nanosphere matrix, and this was followed by calcination to achieve hollow silica–silica nanocomposites. A schematic illustration of the synthesis is shown in Figure 2. The reasons for the incorporation of ACSS into the silica nanosphere matrix will be explained later in more detail. A control sample of the porous silica SLAR coating with an open-pore structure was fabricated on a glass substrate.

Preparation of Sols. First, 0.075 g of PAA was dissolved in 3 mL of ammonium hydroxide, and this solution was subsequently added into 50 mL of anhydrous ethanol ($\text{C}_2\text{H}_5\text{OH}$, EtOH). This was followed by the injection of five aliquots of tetaethylorthosilicate ($\text{Si}(\text{OC}_2\text{H}_5)_4$, TEOS) totaling 0.5 mL; the aliquots were added at intervals of 1 h, under vigorous magnetic stirring at room temperature. After 10 h, a light blue colloid containing 40 nm silica nanospheres filled with the PAA (with an average molecular weight of 3,000) template were formed. The ACSS was prepared via the hydrolysis of TEOS in the presence of a catalyst, hydrochloric acid (HCl), at room temperature. The molar ratios used in the synthesis were TEOS:HCl:H₂O:EtOH = 1:1.7 × 10⁻³:4:40. After stirring for 4 h, the sol was aged for four days. An alkali-catalyzed silica sol was also synthesized using an ammonia catalyst to prepare a porous silica SLAR coating as a control sample, where the molar ratios of TEOS:N-H₃O:EtOH were 0.25:0.75:45.

Fabrication of SLAR Coatings. The SLAR coatings were prepared using a SYDC-200 dip-coating machine. The 2 mm-thick

solar glass slides ($75 \times 25 \text{ mm}^2$) from China Southern Glass were used as substrates. Before dip-coating, the glass substrates were washed twice using detergent, followed by ultrasonic cleaning using water and ethanol for 10 min each. The silica nanospheres filled with the PAA template were deposited on the glass substrate with a withdrawal speed of 2.8 mm/s. After the samples were dried for 10 min in air, the ACSS was subsequently coated on the PAA-filled silica nanospheres using a withdrawal speed of 1.2 mm/s. Finally, the PAA template was removed via calcination in air (performed at 300–450 °C for 1 h) to form the hollow silica–silica nanocomposite SLAR coatings. A control sample of the porous silica SLAR coating was fabricated on a glass substrate with a withdrawal speed of 1 mm/s using the alkali-catalyzed silica sol; the calcination was performed at the same temperature.

Characterization of the Microstructure and Morphology. After being calcined for 1 h, the HSNs were characterized using a field emission transmission electron microscope (FE-TEM, FEI Tecnai F20) to confirm the structure of the hollow nanospheres. The microstructure and surface morphology were investigated using a scanning electron microscope (SEM, Hitachi S-4800) and an atomic force microscope (AFM, CSPM 5500, Benyuan Nano).

Optical Measurements. The refractive index and the extinction coefficient of the deposited thin films and solar glass substrates were determined via the spectroscopic ellipsometry measurements (M2000-DI, J. A. Woollam Co.) using a Cauchy model.²⁴ The optical transmittance and reflectance spectra were measured using an ultraviolet–visible–near-infrared (UV–vis–NIR) spectrophotometer (Lambda950, Perkin-Elmer) with an integrating sphere attached and the resolution was 1 nm for a wavelength range from 300 to 1200 nm.

Optical Simulations. According to the solar spectral irradiance at Air Mass 1.5 (AM1.5, ASTM G173–03),⁴² T_{PV} was calculated as a function of thickness and refractive index for the two-sided coated ideal SLAR coatings on solar glass using a 4×4 propagation matrix method.^{43,44} The optical constants for the bare solar glass, including the refractive index and the extinction coefficient, were determined experimentally via the spectroscopic ellipsometry measurements.

HAST Evaluation. The HAST (PC-422R8, Hirayama) was carried out at a temperature of 121 °C, a relative humidity (RH) of 97%, and a gauge pressure of 0.1 MPa. In this accelerated mode, a test equivalent to a 1000 h damp heat test (85 °C and 85% RH) could be completed within only tens of hours.

Measurements of the Mechanical Properties. The elastic modulus and hardness of the coatings were determined using a nano indenter (NANO G200, MTS). Before performing any indentation, the indenter was stabilized so that the thermal drift rate was less than 0.05 nm/s. For all indentations, a constant strain rate (0.05 s⁻¹) loading was used. For each sample, a 2×2 array with a size of $50 \times 50 \mu\text{m}^2$ was scanned and statistically analyzed.

The abrasion tests were performed using a wet abrasion scrub tester (JTX-II, Pushen). Before starting the tests, the brush was dipped in washing liquid with a pH value of 9.5–11.0 for 20 min. The samples were scrubbed by the brush with a scrub rate of 37 times/min. The 1000 scrub cycles were applied to each side. The abrasion resistance was evaluated by comparing the T_{PV} values before and after the tests.

Time-Dependent WCA and Anti-Fogging Measurements. The water contact angle was measured using an optical contact angle system (OCA 20, Dataphysics) with a droplet volume of 2 μL . The temporal evolution was recorded using a CCD camera with a frame rate of 50 frames per second. The antifogging behavior was assessed by keeping the silica–silica nanocomposite SLAR coatings at a temperature of –15 °C for 3 h, and then exposing them to the ambient laboratory air (RH: 30–50%).

RESULTS AND DISCUSSION

ACSS Infiltration as a Binder and Regulator. In this synthesis protocol, the PAA, which acted as a template, was first enclosed by silica, and then removed via calcination. The shell of thickness was controlled by varying the amount of TEOS used, and the ratio of PAA to ethanol determined the particle size^{33,34} (see the Supporting Information, Figure S1, which

shows the variation in the particle size by varying the amount of PAA). As shown in Figure 3a, the synthesized HSNs had a

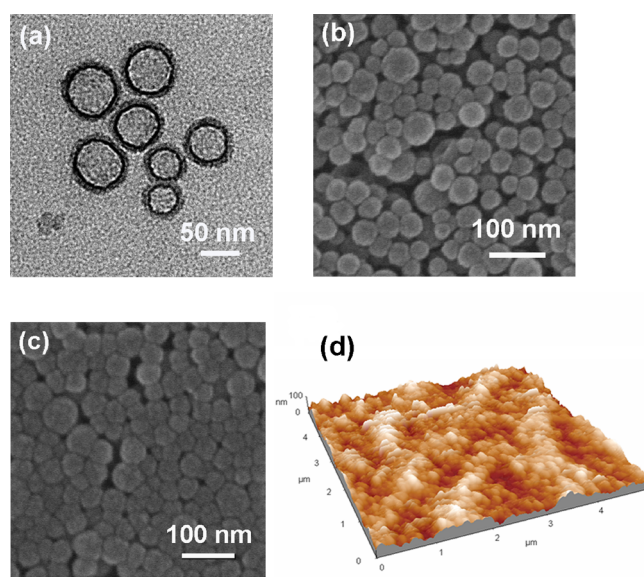


Figure 3. (a) TEM image of the HSNs. (b) SEM image of the surface morphology of a thin film consisting solely of HSNs. (c) SEM image of the silica–silica nanocomposite SLAR coating consisting of HSNs and ACSS, which reveals low porosity. (d) Corresponding 3D AFM image of the nanocomposite SLAR coating.

mean diameter of 40 nm and a shell thickness of 5 nm. The surface morphology of the HSNs-based thin films is shown in Figure 3b; the HSNs were uniformly distributed with the gaps on the order of tens of nanometers. The refractive index of the film was approximately 1.15 at a wavelength of 500 nm (see Supporting Information, Figure S2), much lower than that of the ideal SLAR coating, $n = (n_{\text{air}}n_{\text{glass}})^{1/2} \approx 1.23$. The relationship between the refractive index and the porosity can be described as follows⁴⁵

$$n_p^2 = (n^2 - 1) \left(1 - \frac{P}{100} \right) + 1 \quad (2)$$

where n_p and n are the refractive indices of porous and nonporous materials, respectively, and P represents the percentage porosity. Considering that n was constant ($n = 1$ for the pores in the hollow silica nanosphere (HSN) films), eq 2 suggested that the way to increase the refractive index of the HSN films was to reduce the porosity, P ; that is, the gaps between the HSNs should be partially filled.

ACSS tends to produce linearly or randomly branched chain molecules.⁴⁶ This behavior could have been responsible for the formation of the dense films with a high refractive index of 1.46 at a wavelength of 500 nm (see the Supporting Information, Figure S2). In our experiments, we chose ACSS to fill the gaps surrounding the HSNs, resulting in the formation of silica–silica nanocomposite SLAR coatings. As shown in Figure 3c, the ACSS penetrated the gaps between the HSNs such that the gaps were substantially filled after infiltration with the ACSS, in contrast with those shown in Figure 3b. This bridging of the gaps suggested that the mechanical properties of the nanocomposite SLAR coatings would likely be strengthened. In addition, the nanocomposite SLAR coating showed a root-

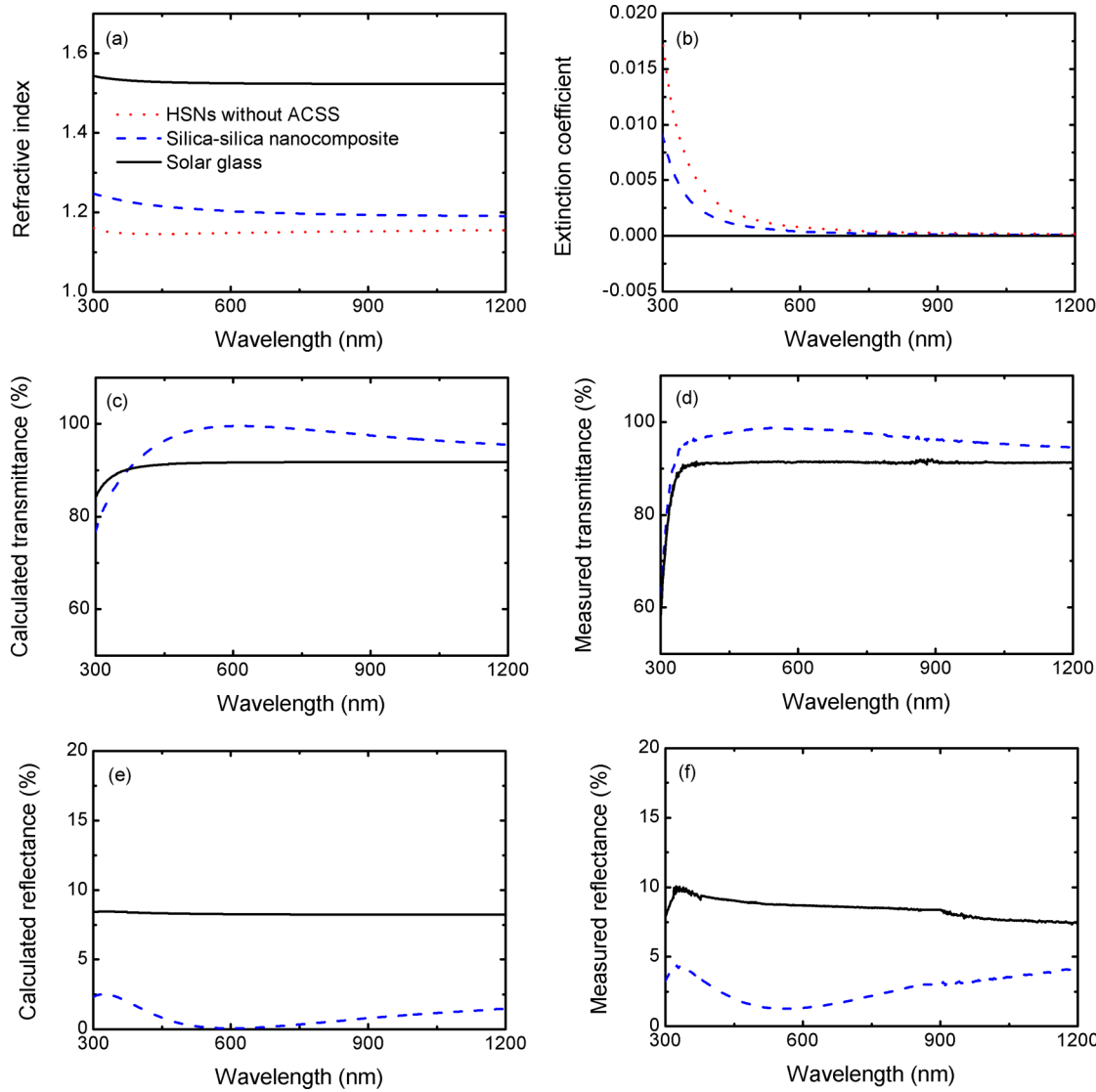


Figure 4. (a) Experimentally determined refractive indices and (b) extinction coefficients of the HSN thin film, silica–silica nanocomposite SLAR coating, and solar glass substrate. (c) Calculated and (d) measured transmittance spectra of the nanocomposite SLAR coating and the bare substrate. (e) Calculated and (f) measured reflectance spectra of the nanocomposite SLAR coating and the bare substrate.

mean-square roughness of 14.4 nm, as determined from the AFM measurements (see Figure 3d). This surface roughness had the potential to have an impact on the wettability, as suggested by the Wenzel equation.⁴⁷

Besides bridging the gaps between the HSNs, ACSS also played a role in tuning the refractive index. The optical constants of the silica–silica nanocomposite SLAR coatings, determined using the spectroscopic ellipsometry measurements, are plotted with the values for the solar glass substrate in panels a and b in Figure 4. These figures indicated that the refractive index of the nanocomposite SLAR coating had an increased value of 1.21 at a wavelength of 500 nm, compared with that of the HSN film without the infiltration of ACSS, 1.15. This value was very close to that of the ideal SLAR coating, 1.23. In contrast, the extinction coefficient decreased, as shown in Figure 4b; this was attributed to the infiltration of ACSS into the HSN film, which resulted in a smoothening of the surface of the film. Hence, the scattering loss was suppressed. This also suggested that the refractive index of the silica–silica nanocomposite SLAR coatings could be tuned

to some extent by controlling the amount of ACSS used (i.e., the withdrawal speed of ACSS during the process of infiltrating the ACSS into the HSN films).

AR Properties. Panels c and d in Figure 4 show the calculated and the measured transmittance spectra of a silica–silica nanocomposite SLAR coating with a thickness of 125 nm that was calcined at 450 °C, compared with the spectra of the bare glass. The reflectance spectra are shown in panels e and f in Figure 4. The measurements were in good agreement with the calculations, especially at wavelengths longer than 600 nm. The discrepancies at short wavelengths were ascribed to the deviation of the extracted optical constants in this wavelength regime. It should be noted that the calculated reflectance was smaller than the measured value for the silica–silica nanocomposite SLAR coatings within the range of wavelengths investigated in this study. We believe that small differences between the numerically extracted and the real refractive indices and small variations in the thickness likely gave rise to the observed disparity, because the reflectance of the nanocomposite SLAR coating itself was rather low. In contrast,

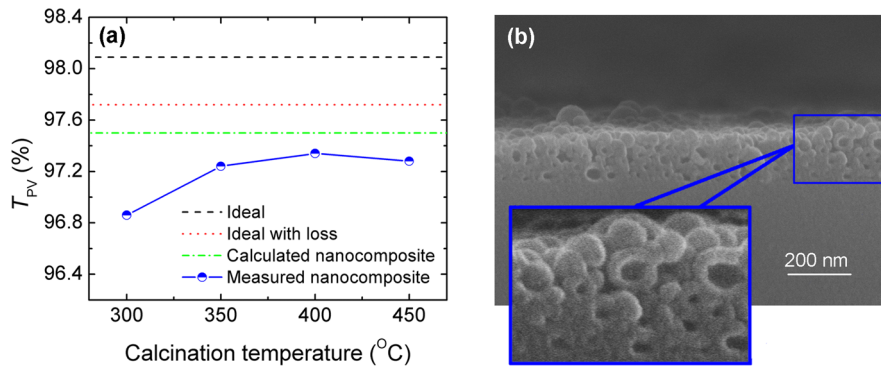


Figure 5. (a) Variation in T_{PV} under different calcination temperatures from 300 to 450 °C. The ideal cases with and without loss, and the calculated nanocomposite SLAR coatings had T_{PV} values of 97.72, 98.09, and 97.50%, respectively. (b) Cross-sectional SEM image of the silica–silica nanocomposite SLAR coating after calcination at 450 °C.

the calculated and the measured transmittance of the bare solar glass showed no significant differences in the range of wavelengths investigated, as summarized in Table 1. The calculated and the measured R_{PV} values of the bare solar glass were 8.28 and 8.56%, respectively, whereas the nanocomposite SLAR coating had a measured R_{PV} of 2.27%, which was much higher than the calculated value of 0.61%. Although the R_{PV} value was overestimated in the calculations for the nanocomposite SLAR coating, the experimental results showed a significant reduction in the reflectance (6.29%) and a significant improvement in the transmittance (6.07%), compared with the bare solar glass. Furthermore, the antireflective properties were affected less by the variation of the calcination temperature from 300 to 450 °C, as illustrated in Figure 5a and in the Supporting Information (see Figure S4 and Table S1). It was found that T_{PV} increased with the increases in the calcination temperature, which facilitated the removal of the PAA template. When the calcination temperature reached 400 °C, T_{PV} approached the maximum value, close to the calculated value. No apparent improvement in T_{PV} was observed when the temperature was increased further, because the PAA template had been completely eliminated, as shown in Figure 5b. The cross-sectional SEM image in Figure 5b shows the nanocomposite SLAR coating calcined at 450 °C, in which mostly closed-pore shells were observed. When the coating was calcined at a lower temperature (e.g., 300 °C), the HSNs could also be produced (see the Supporting Information, Figure S3a). However, the closed-pore shells containing PAA cores exhibited solid sphere characteristics in the cross-sectional SEM image (see the Supporting Information, Figure S3b).

Durability in Damp Heat Environments. Regarding the practical use of such silica–silica nanocomposite SLAR coatings in PV modules, it is important to establish whether such coatings have high T_{PV} , and whether they can withstand severe weather, especially high temperatures and humid environments. According to the module test protocol adopted by the International Electrotechnical Commission (IEC), IEC 61215,⁴⁸ PV modules must be able to withstand 1000 h of damp heat tests (85 °C and 85% RH); this protocol is also typically used to evaluate the durability of AR coatings as well.^{16,49,50} In our experiments, an accelerated-aging test, HAST, was performed. The acceleration factor of HAST relative to the damp heat test at 85 °C and 85% was estimated using the equation below⁵¹

$$AF = \exp \left[\frac{E_a}{k} \left(\frac{1}{T_u} - \frac{1}{T_s} \right) + (RH_u^n - RH_s^n) \right] \quad (3)$$

where AF is the acceleration factor, E_a is the activation energy in eV, k is the Boltzmann constant, 8.6×10^{-5} . The T_u and T_s values represent the temperatures of the standard damp heat test and the HAST, respectively. RH_u and RH_s denote the humidity in the standard test and the HAST, respectively. E_a and n are typically taken to be 1.3 and 2, respectively. According to the relationship in eq 3, a test equivalent to a 1000 h damp heat test can be performed via tens of hours of HAST.^{52,53} As a control experiment, a porous silica SLAR coating was also optimized and deposited on the solar glass, achieving a T_{PV} of 96.38% and a R_{PV} of 3.39% (the optical spectra and the SEM image of the surface micrography are shown in Figure S5 in the Supporting Information); these values were comparable with the values reported in the literature.^{17,20} Figure 6 shows the normalized variation in T_{PV} as

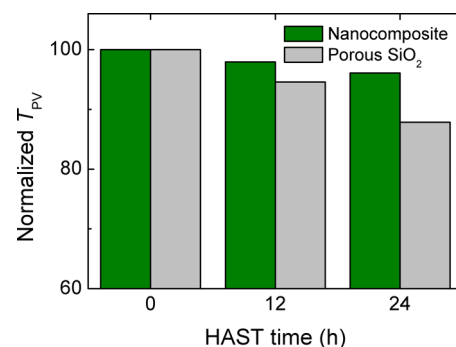


Figure 6. Comparison of the degradation in the normalized T_{PV} as a function of HAST time, shown for the silica–silica nanocomposite and porous silica SLAR coatings.

a function of the HAST time for the silica–silica nanocomposite SLAR and the porous silica SLAR coatings. After a 12 h HAST, the normalized T_{PV} values for the porous silica SLAR and the nanocomposite SLAR coatings decreased to 94.59 and 97.92% of the initial values, respectively. The degradation was more evident for the porous silica SLAR coatings after experiencing a 24 h HAST. The normalized T_{PV} of the porous silica SLAR coating dropped to 87.86%, whereas that of the nanocomposite SLAR coating was well preserved at 96.08%. These results confirmed that the closed-pore SLAR

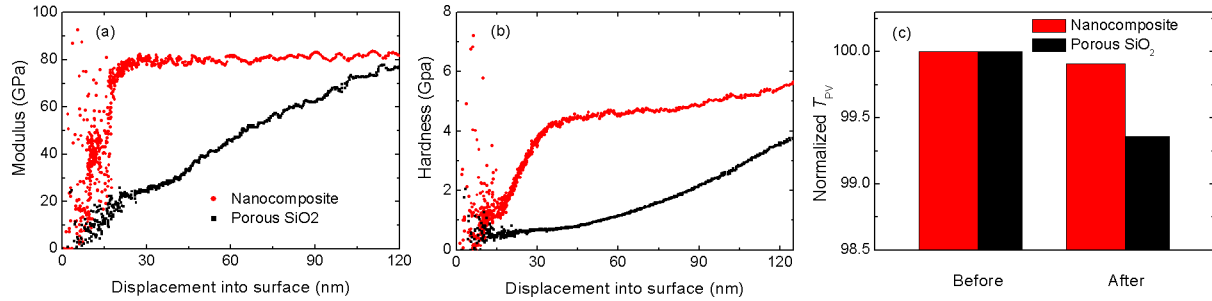


Figure 7. Nanoindenter and abrasion test results for the silica–silica nanocomposite SLAR coating (as indicated in red), and the control sample, the porous silica SLAR coating (as indicated in black). (a) Elastic modulus and (b) hardness as a function of displacement into the surface, and (c) degradation of the normalized T_{PV} after 1000 scrub cycles on each side of the samples.

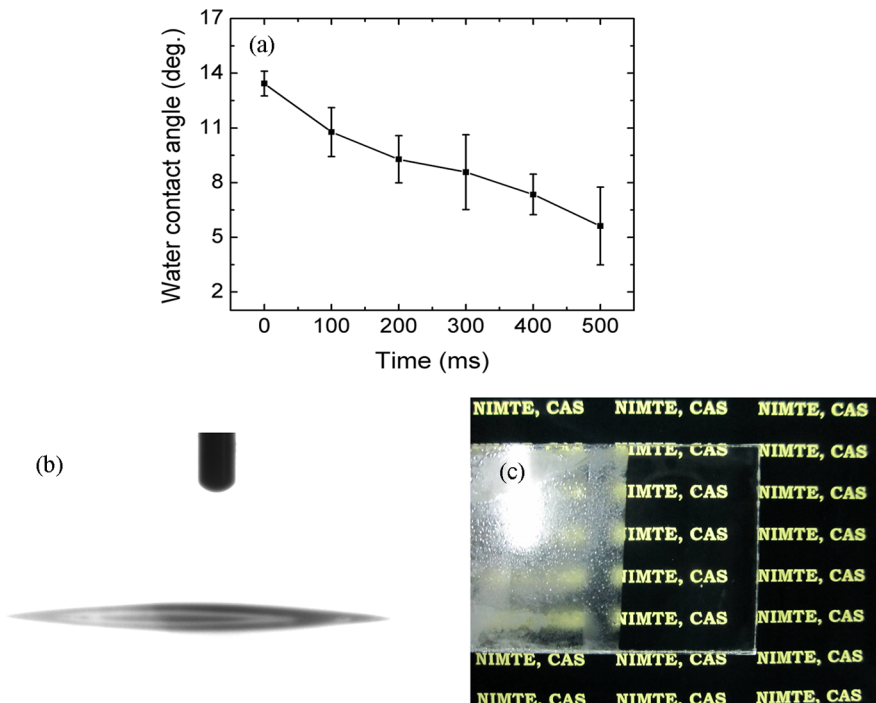


Figure 8. (a) Time-dependent WCA results for a 2 μ L water droplet. (b) Snapshot of a water droplet on the silica–silica nanocomposite SLAR coating surface after 0.5 s. (c) Photograph of printed letters as seen through the uncoated glass part (left) and the silica–silica nanocomposites coated part (right).

coatings had excellent resistance to moisture at high temperatures; these structures were able to circumvent the infiltration of water more effectively, because of the lower porosity on their surface.

Mechanical Performance. Besides the ability to resist moisture, the mechanical durability was also investigated using nanoindenter measurements to provide quantitative information on the elastic modulus, E , and hardness, H , based on the conventional Oliver-Pharr method. Although films thicker than 500 nm are preferred in nanoindenter measurements, Berasategui et al.⁵⁴ have demonstrated that the nanoindentation technique can also be applied to AR coatings thinner than 100 nm. Panels a and b in Figure 7 show the elastic modulus and the hardness, respectively, of the nanocomposite and the porous silica SLAR coatings. The significant variations of the modulus and the hardness between 0 and 13 nm of displacement into the surface were ascribed to the surface roughness;⁵⁵ these results were consistent with the root-mean-square roughness of 14.4 nm that was measured using AFM. The hardness versus displacement curve for the silica–silica

nanocomposite SLAR coatings showed that a more stable hardness was achieved when the displacement into the surface was larger than 15 nm. The plateau values, 0.6 and 1.6 GPa, could be considered as the hardness of the porous and nanocomposite SLAR coatings, respectively, where the displacement was approximately 15 nm (around 10% of the film thickness). The increase in the hardness value for the silica–silica nanocomposite SLAR coatings, compared with the porous SLAR coatings, was attributed to the infiltration of the ACSS into the gaps between the HSNs and the thermal treatment. These processes strengthened the nanocomposite coatings and improved the hardness, which was comparable with that of BEA zeolite³ and even alumina atomic-layer-deposition treated TiO₂/SiO₂ LBL films.⁵⁵ In addition, the silica–silica nanocomposite SLAR coatings also demonstrated the advantage of abrasion resistance over the porous SLAR coatings, as shown in Figure 7c; the silica–silica nanocomposite SLAR coatings retained a normalized T_{PV} of 99.91%, a degradation less than 0.1%, while the normalized T_{PV} of the

porous SLAR coatings decreased to 99.36% after 1000 scrub cycles on each side.

Surface Wettability. It is known that the volume fraction of voids and the surface roughness would significantly affect the wettability, as a result of 3D capillary effects and the Wenzel state.^{29,56–58} The former existed in the form of gaps in the samples, and the latter was confirmed by the AFM measurements. The wettability of the silica–silica nanocomposite SLAR coatings was investigated using time-dependent WCA measurements, as shown in Figure 8a. It was observed that the WCA decreased from 13° to approximately 5° after 0.5 s, which indicated that the nanocomposite SLAR coatings had nearly superhydrophilic and antifogging characteristics.^{29,59} This meant that the water droplets spread rapidly once they reached the surface, as illustrated in Figure 8b and the movie in the Supporting Information. As shown in Figure 8c, many condensed droplets and strong reflections were observed in the uncoated part (left) of the solar glass, whereas fog was hardly present in the silica–silica nanocomposite SLAR coated part (right). Such robust antifogging properties could facilitate the self-cleaning of solar glass,²⁹ because the water droplets would spread and evaporate instantaneously.

CONCLUSIONS

In conclusion, we produced novel silica–silica nanocomposite SLAR coatings by infiltrating ACSS into HSNs, using a sol–gel dip-coating method. By infiltrating ACSS into the HSN matrix as a regulator, the refractive index could be experimentally tuned to give values close to PV-transmittance-oriented design values. As a result, the maximum measured T_{PV} reached 97.34%, close to the theoretical limit for lossy SLAR coatings of 97.72%. In addition to the excellent antireflective properties, the closed-pore structure in the silica–silica nanocomposite SLAR coatings resulted in a strong resistance to moisture at high temperatures; the T_{PV} value was maintained at 96.08% of the initial value even after a severe, 24 h HAST evaluation that was equivalent to a 1000 h damp heat test at 85 °C and 85% RH, whereas the normalized T_{PV} of the open-pore porous silica SLAR coating decreased significantly, to 87.86%. The nanocomposite SLAR coating had a hardness of approximately 1.6 GPa, far superior to the values of 0.6 GPa shown by the open-pore silica SLAR coating; this was due to the infiltration of ACSS, which bridged the gaps in the HSN films, thus densifying the coatings. The nanocomposite SLAR coating was hardly affected by abrasion, and the degradation in T_{PV} was less than 0.1%, while the open-pore silica SLAR coating had a degradation value of more than 0.6%. Furthermore, a WCA of approximately 5° was observed after 0.5 s, because of the appropriate volume fraction of voids and surface roughness, resulting in the desirable antifogging and self-cleaning characteristics. The ACSS-infiltrated closed-pore nanocomposite SLAR coatings produced in this study showed high transparency, good durability, and nearly superhydrophilic (antifogging) properties, and they were simple to fabricate; these coatings have potential to be applied in energy harvesting and optical instrumentation in extreme climates or humid conditions.

ASSOCIATED CONTENT

Supporting Information

Experimental details, optical spectra at different calcination temperatures, and results of time-dependent WCA measur-

ements. This material is available free of charge via the Internet at <http://pubs.acs.org/>.

AUTHOR INFORMATION

Corresponding Authors

*E-mail: yhlu@nimte.ac.cn. Phone: +86 (0)574 87913375. Fax: +86 (0)574 87913375.

*E-mail: weijiesong@nimte.ac.cn

Notes

The authors declare no competing financial interest.

ACKNOWLEDGMENTS

This work was supported by the National Natural Science Foundation of China (11104290, 51102250, 11204146, 11211140338) and the Ningbo Key Innovation Team (2011B82005, 2009B21005).

REFERENCES

- (1) Thelen, A. *Design of Optical Interference Coatings*; McGraw-Hill: New York, 1988.
- (2) Macleod, H. A. *Thin-Film Optical Filters*; Institute of Physics Publishing: Philadelphia, PA, 2001.
- (3) Chen, C.-H.; Li, S.-Y.; Chiang, A. S. T.; Wu, A. T.; Sun, Y. S. *Sol. Energy Mater. Sol. Cells* **2011**, *95*, 1694–1700.
- (4) Chevallier, P.; Turgeon, S.; Sarra-Bournet, C.; Turcotte, R.; Laroche, G. *ACS Appl. Mater. Interfaces* **2011**, *3*, 750–758.
- (5) Son, J.; Kundu, S.; Verma, L. K.; Sakhija, M.; Danner, A. J.; Bhatia, C. S.; Yang, H. *Sol. Energy Mater. Sol. Cells* **2012**, *98*, 46–51.
- (6) Green, M. A. *Silicon Solar Cells: Advanced Principles and Practice*; Centre for Photovoltaic Devices and Systems: Sydney, 1995.
- (7) Jorgensen, G. J.; Terwilliger, K. M.; Cueto, J. A. D.; Glick, S. H.; Kempe, M. D.; Pankow, J. W.; Pern, F. J.; McMahon, T. J. *Sol. Energy Mater. Sol. Cells* **2006**, *90*, 2739–2775.
- (8) Willey, R. R. *Appl. Opt.* **1993**, *32*, 5447–5451.
- (9) Yan, X.; Poxson, D. J.; Cho, J.; Welser, R. E.; Sood, A. K.; Kim, J. K.; Shubert, E. F. *Adv. Funct. Mater.* **2012**, *23*, 583–590.
- (10) Zhang, X.-X.; Cai, S.; You, D.; Yan, L.-H.; Lv, H.-B.; Yuan, X.-D.; Jiang, B. *Adv. Funct. Mater.* **2013**, *23*, 4361–4365.
- (11) Minot, M. J. *J. Opt. Soc. Am.* **1976**, *66*, 515–519.
- (12) Southwell, W. H. *Opt. Lett.* **1983**, *8*, 584–586.
- (13) Xi, J.-Q.; Schubert, M. F.; Kim, J. K.; Schubert, E. F.; Chen, M.; Lin, S.-Y.; Liu, W.; Smart, J. A. *Nat. Photonics* **2007**, *1*, 176–179.
- (14) Choi, K.; Park, S. H.; Song, Y. M.; Lee, Y. T.; Hwangbo, C. K.; Yang, H.; Lee, H. S. *Adv. Mater.* **2010**, *22*, 3713–3718.
- (15) Shin, J.-H.; Han, K.-S.; Lee, H. *Prog. Photovolt.: Res. Appl.* **2011**, *19*, 339–344.
- (16) Ballif, C.; Dicker, J.; Borchert, D.; Hofmann, T. *Sol. Energy Mater. Sol. Cells* **2004**, *82*, 331–344.
- (17) Lu, X.; Wang, Z.; Yang, X.; Xu, X.; Zhang, L.; Zhao, N.; Xu, J. *Surf. Coat. Technol.* **2011**, *206*, 1490–1494.
- (18) Barranco, A.; Contrino, J.; Yubero, F.; Espinos, J. P.; Gonzalez-Elipe, A. R. *J. Vac. Sci. Technol. A* **2004**, *22*, 1275–1284.
- (19) Guillemot, F.; Brunet-Bruneau, A.; Bourgeat-Lami, E.; Gacoin, T.; Barthel, E.; Boilot, J.-P. *Chem. Mater.* **2010**, *22*, 2822–2828.
- (20) Karasinski, P.; Jaglarz, J.; Reben, M.; Skoczek, E.; Mazur, J. *Opt. Mater.* **2011**, *33*, 1989–1994.
- (21) Moghal, J.; Kobler, J.; Sauer, J.; Best, J.; Gardener, M.; Watt, A. A. R.; Wakefield, G. *ACS Appl. Mater. Interfaces* **2012**, *4*, 854–859.
- (22) Cooper, G. I.; Cox, G. A. *Appl. Geochem.* **1996**, *11*, 511–521.
- (23) Vilarigues, M.; da Silva, R. C. *J. Non-Cryst. Solids* **2006**, *352*, 5368–5375.
- (24) Lee, D.; Rubner, M. F.; Cohen, R. E. *Nano Lett.* **2006**, *6*, 2305–2312.
- (25) Chhajed, S.; Schubert, M. F.; Kim, J. K.; Schubert, E. F. *Appl. Phys. Lett.* **2008**, *93*, 251108.
- (26) Liu, Z.; Zhang, X.; Murakami, T.; Fujishima, A. *Sol. Energy Mater. Sol. Cells* **2008**, *92*, 1434–1438.

(27) Willey, R. R. *Appl. Opt.* **2011**, *50*, C86–C89.

(28) Shimomura, H.; Gemici, Z.; Cohen, R. E.; Rubner, M. F. *ACS Appl. Mater. Interfaces* **2010**, *2*, 813–820.

(29) Li, X.; Du, X.; He, J. *Langmuir* **2010**, *26*, 13528–13534.

(30) Yang, Z. H.; Cong, H. L.; Cao, W. X. *J. Polym. Sci., Part A: Pol. Chem.* **2004**, *42*, 4284–4288.

(31) Zoldesi, C. I.; Imhof, A. *Adv. Mater.* **2005**, *17*, 924–928.

(32) Chen, M.; Wu, L.; Zhou, S.; You, B. *Adv. Mater.* **2006**, *18*, 801–806.

(33) Wan, Y.; Yu, S. *J. Phys. Chem. C* **2008**, *112*, 3641–3647.

(34) Du, Y.; Luna, L. E.; Tan, W. S.; Rubner, M. F.; Cohen, R. E. *ACS Nano* **2010**, *4*, 4308–4316.

(35) Du, X.; He, J. *Chem.—Eur. J.* **2011**, *17*, 8165–8174.

(36) Park, K.-C.; Choi, H. J.; Chang, C.-H.; Cohen, R. E.; McKinley, G. H.; Barbastathis, G. *ACS Nano* **2012**, *6*, 3789–3799.

(37) Min, W.-L.; Jiang, B.; Jiang, P. *Adv. Mater.* **2008**, *20*, 3914–3918.

(38) Guldin, S.; Kohn, P.; Stefk, M.; Song, J.; Divitini, G.; Ecarla, F.; Ducati, C.; Wiesner, U.; Steiner, U. *Nano Lett.* **2013**, *13*, 5329–5335.

(39) Xu, L.; He, J.; Yao, L. *J. Mater. Chem. A* **2014**, *2*, 402–409.

(40) Helsch, G.; M os, A.; Deubener, J.; H oland, M. *Sol. Energy Mater. Sol. Cells* **2010**, *94*, 2191–2196.

(41) Li, D.; Huang, F.; Ding, S. *Appl. Surf. Sci.* **2011**, *257*, 9752–9756.

(42) ASTM G173–03, *Standard Tables for Reference Solar Spectral Irradiances*; ASTM International: West Conshohocken, PA, 2005.

(43) Abdulhalim, I. *J. Opt. A: Pure Appl. Opt.* **1999**, *1*, 646–653.

(44) Lu, Y. H.; Huang, M. D.; Park, S. Y.; Kim, P. J.; Lee, Y. P.; Rhee, J. Y.; Hwango, C. K.; Chen, L. Y. *J. Appl. Phys.* **2007**, *101*, 103103.

(45) Yoldas, B. E. *Appl. Opt.* **1980**, *19*, 1425–1429.

(46) Ye, H.; Zhang, X.; Zhang, Y.; Ye, L.; Xiao, B.; Lv, H.; Jiang, B. *Sol. Energy Mater. Sol. Cells* **2011**, *95*, 2347–2351.

(47) Yu, X.; Wang, Z.; Jiang, Y.; Zhang, X. *Langmuir* **2006**, *22*, 4483–4486.

(48) IEC 61215: *Crystalline Silicon Terrestrial Photovoltaic (PV) Modules—Design Qualification and Type Approval*; International Electrotechnical Commission (IEC): Geneva, Switzerland, 2005.

(49) Li, J.; Lan, P.; Xu, H.; Zhang, X.; Yang, Y.; Tan, R.; Jylhä, O.; Lu, Y. *J. Appl. Phys.* **2012**, *112*, 093517.

(50) Li, J.; Lu, Y.; Lan, P.; Zhang, X.; Xu, W.; Tan, R.; Song, W.; Choy, K.-L. *Sol. Energy* **2013**, *89*, 134–142.

(51) *Manual of the Highly-Accelerated Temperature and Humidity Stress Test (HAST)*; Hirayama: Kasukabe-shi, Japan, 2010.

(52) JESD22-A118, *Accelerated Moisture Resistance-Umbiased HAST*; JEDEC Solid State Technology Association: Arlington, VA, 2000.

(53) JESD22-A110-B, *Highly-Accelerated Temperature and Humidity Stress Test (HAST)*; Electronic Industries Alliance/JEDEC Solid State Technology Association: Arlington, VA, 1999.

(54) Berasategui, E.; Bull, S. J.; Page, T. F. *Thin Solid Films* **2004**, *447*, 26–32.

(55) Dafinone, M. I.; Feng, G.; Brugarolas, T.; Tettey, K. E.; Lee, D. *ACS Nano* **2011**, *5*, 5078–5087.

(56) Wenzel, R. N. *Ind. Eng. Chem.* **1936**, *28*, 988–994.

(57) Bico, J.; Marzolin, C.; Quéré, D. *Europhys. Lett.* **1999**, *47*, 220–226.

(58) Bico, J.; Tordeux, C.; Quéré, D. *Europhys. Lett.* **2001**, *55*, 214–220.

(59) Li, X.; He, J. *ACS Appl. Mater. Interfaces* **2012**, *4*, 2204–2211.